SOFT ROBOTS

Multimodal information structuring with single-layer soft skins and high-density electrical impedance tomography

David Hardman[1]*, Thomas George Thuruthel[2], Fumiya Iida[1]

The human skin can reliably capture a wide range of multimodal data over a large surface while providing a soft interface. Artificial technologies using microelectromechanical systems (MEMS) can emulate these biological functions but present numerous challenges in fabrication, delamination due to soft-rigid interfaces, and electrical interference. To address these difficulties, we present a single-layer multimodal sensory skin made using only a highly sensitive hydrogel membrane. Using electrical impedance tomography techniques, we accessed up to 863,040 conductive pathways across the membrane, allowing us to identify at least six distinct types of multimodal stimuli, including human touch, damage, multipoint insulated presses, and local heating. Through comprehensive physical testing, we demonstrate that the highly redundant and coupled sensory information from these pathways can be structured using data-driven techniques, selecting which pathways should be monitored for efficient multimodal perception. To demonstrate our approach's versatility, we cast the hydrogel into the shape and size of an adult human hand. Using our information structuring strategy, we demonstrate the hand's ability to predict environmental conditions, localize human touch, and generate proprioceptive data. Our framework addresses the challenge of physically extracting meaningful information in multimodal soft sensing, opening new directions for the information-led design of single-layer skins in sensitive systems.

INTRODUCTION

Human skin provides us with a large amount and variety of sensory information. Creating similar artificial skins for robotic systems is challenging not only in the physical design space but also at the computational level (*1*–*4*). Many skins and soft sensing interfaces have been designed to respond to light contact (*5*–*10*). Such single-modality sensing is essential for robots to perform complex tasks (*11*) but does not capture the full functionality of human skins—such as temperature, pressure, and damage sensing. As we design more functional robots, the need for multimodal perception in soft skins continues to grow (*12*).

Electronic skins transform physical information into electronic signals using a combination of functional materials, mechanisms, and device architectures (*13*–*15*). Multimodality is typically obtained by combining sensing units with stimuli-specific responses (*16*, *17*); many existing robotic skins rely on the integration of modular sensory components embedded in a flexible, soft substrate (*18*–*25*). Although such skins show promise as wearable sensing technologies, they are still not well suited for robotic applications for several reasons. First, their fabrication is tedious because of the need to distribute and wire multiple small components over a large surface, limiting them to simple shapes. Because of the presence of multiple soft-rigid interfaces, the skins are typically not stretchable or are highly prone to damage. Last, there is the challenge of signal interference and cross-talk, which reduces accuracy (*12*, *26*).

Another technique for measuring multimodal sensory information, which is rarely found in literature, is to use the same sensing unit for all stimuli, with different responses corresponding to different stimuli. This approach presents challenges in decoupling the corresponding stimuli but vastly simplifies fabrication and uses fewer soft/rigid interfaces. Decoupling and distinguishing the external stimuli are then achieved using high-throughput sensory channels and computational techniques that exploit redundancies in information (*27*, *28*). Vision-based tactile skins are one such sensing mechanism that allows high-density sensory information, which can be used for multimodal perception (*27*, *29*, *30*). However, vision-based sensors are limited to simple shapes and are prone to damage because of soft-rigid interfaces (refer to table S2 for a comparison of the state-of-the-art tactile skins).

Recently, electrical impedance tomography (EIT) has emerged as a method for sensorizing continuous conductive materials like fabrics and hydrogels (*31*–*37*). Electrodes are positioned over the material or around its perimeter, and selected tetrapolar electrode configurations are used for multiplexed impedance measurements. With increasing electrode count, numerous configurations arise. By selecting configurations on the basis of the generated electric fields across soft skin, the method's output can be structured, balancing sampling rate and information content (*38*, *39*). Traditionally, electrode selection has depended on analytic reconstruction methods, but with the rise of machine learning in sensory data processing (*35*, *40*), more possibilities are available.

Previous works have explored data-driven selection of EIT drive electrodes, often considering adjacent, opposite, and trigonometric configurations (*34*, *41*, *42*), mainly through simulation-based analyses (*43*, *44*). Direct physical testing can identify excitation patterns better suited to the application (*45*), without simulation-to-reality (Sim2Real) discrepancies. However, physical experiments are more time consuming than their simulated equivalents. By comparing the information returned from every possible electrode configuration in our physical sensory system, we used a data-driven approach to return multimodal data with maximum information content. By monitoring all possibilities, we could identify which configurations provided the most information about particular sensory stimuli, enabling efficiency in subsequent system implementations by monitoring

[1]Bio-Inspired Robotics Lab, University of Cambridge, Cambridge, UK. [2]Department of Computer Science, University College London, London, UK.
*Corresponding author. Email: dsh46@cam.ac.uk

only these channels. We focused on techniques that could be directly applied to a range of complex-shaped multimodal skins without the need for finite element simulations. Although traditional EIT solvers first aim to reconstruct a system's conductivity map, we instead output the sensory stimuli directly: type, location, temperature, and humidity.

By monitoring every configuration, we were not limited by the traditional assumptions of reciprocity, measurement interdependence, and frequency independence (*46*), and we were instead able to directly identify a system's optimal configurations for specific sensing modalities. Such an approach allows for complex physical setups in which these assumptions may not hold perfectly; even when they do, our data-driven approach can exploit the subsequent information redundancies to generate its predictions from noisy data sources, operating close to idealized limits of information content.

A limited number of works has explored the application of EIT for multimodal robotic sensing, including applications for human touch, temperature sensing, and gesture recognition (*31*, *47*, *48*). We have previously shown that a circular two-dimensional (2D) skin trained to recognize only single presses could make reasonable predictions of multipress deformations and damage states while simultaneously monitoring the environment's temperature and humidity (*49*). However, existing approaches have been limited to simple skin shapes because of the challenges involved in using standard EIT devices for complex 3D shapes (*50*); even shell structures, which are topologically equivalent to circular 2D skins, will produce weaker responses to a given stimulus because of the increased length of their current paths. Zhang and Harrison (*51*) used 28 configurations of electrodes placed around a human's wrist to differentiate between hand gestures using machine learning: Although this demonstrated the promising potential of EIT measurements to reconstruct more complex shapes, multimodal stimuli were not considered.

In this work, we aimed to develop tactile skin technologies that can be seamlessly integrated into existing robotic devices while providing high-density multimodal tactile information. To do so, we explored the information structuring of high-density EIT on complex-shaped single-layer sensorized membranes that respond to multimodal tactile cues. Using EIT hardware, we selected electrode combinations that generate specific electric fields across a healable hydrogel developed for soft strain-sensing applications (*52*). The hydrogel's thermoreversibility allows it to be cast into sensorized 3D skins, and we demonstrated our multimodal sensing approach on a full-size hollow hand with electrodes positioned only around its wrist.

We used our approach to balance between the 1.7 million available information channels and a bandwidth of up to 33 kHz by identifying and only monitoring the setup-specific channels providing information most efficiently. In doing so, we demonstrated how the hand could predict environmental temperature and humidity, localize light touches to 25 mm over a 38,000-mm^2 area, and provide proprioceptive data when its fingers were actuated.

Figure 1A presents an overview of our framework for multimodal sensing. A soft sensorized membrane functioned as the skin and was cast from a gelatin-based hydrogel. This hydrogel, presented in (*52*), is low cost and stretchable, piezoresistively responds to strain, and can be used to monitor environmental temperatures and humidities. Its electrical and mechanical properties can be tuned through its composition, enabling application-specific designs. Here, we depict the skin as a circle, but its single-layer thermoreversibility means it can be straightforwardly cast into more complex morphologies, such as a hollow human hand.

To monitor the skin's multimodal interactions, up to 32 electrodes were arranged around its perimeter. Multiple tetrapolar electrode excitation patterns can be quickly swept across these electrodes using EIT electronics: Two electrodes inject an ac to generate an electric field across the membrane, and the resulting voltage difference is measured between two other electrodes. Through various mechanisms, multimodal stimuli cause changes in the electric field, which are recorded by the peripheral electrodes. By carefully selecting the electrode configurations that we use to monitor the skin, the system's output information could be structured to efficiently return modality and application-specific data. We selected these configurations directly from physical measurements, ensuring that our approach can be directly applied to complex physical setups without requiring simulations.

In an idealized system, many of the available configurations are linearly dependent. Instead of assuming our system to be ideal, we considered the signals returned by all possible configurations, ensuring that information was not lost because of small nonlinearities in the electronic circuitry and physical coupling. This approach means that the four electrodes used for each measurement were chosen completely independently, giving 863,040 ($= 32 \times 31 \times 30 \times 29$) possible configurations of 32 electrodes. By measuring the amplitude [as root mean square (RMS)] and phase shift of all ac signals, 1,726,080 information channels were available for data-driven evaluation. At its highest speed, our circuitry can monitor all of these channels at a 0.02-Hz frame rate. By selectively structuring our excitation configurations, this frame rate could be linearly improved to a maximum of 33 kHz (when monitoring one configuration) while providing sufficient information about the form and location of the multimodal stimuli. Using our sensor-specific methodology, we envisage a pipeline for multimodal skin calibration: All available channels are first monitored during a small range of physical tests, which are then used to select a subset of configurations to best strike the balance between speed and information content while accounting for noise, setup imperfections, nonlinearities, and signal redundancies. Unlike existing cutting-edge works (*31*, *47*, *48*), our surfaces can be cast into complex 3D shapes and can respond to multimodal stimuli using only a single-layer structure. We move beyond previous 3D shape sensorization demonstrations—such as humanoid faces (*32*)—by explicitly considering multimodality, incorporating responses from more than 1000 tactile stimuli and 100 hours of environmental monitoring. We first developed our approach and analyzed the material-level responses using an eight-electrode circular membrane of the gelatin-based hydrogel before applying the pipeline to a complex-shaped soft single-layer hand, where we demonstrate its multimodal capabilities.

RESULTS

Multimodality through material-level stimuli response

Figure 1B depicts the membrane on which we first tested our information structuring approaches. A 10-cm-diameter hydrogel circle was surrounded by eight electrodes, providing 1680 potential tetrapolar configurations and 3360 potential information channels. All could be monitored by the high-speed electronics at up to 9.8 Hz (table S1)—we selected a 1-Hz rate to minimize the noise present in

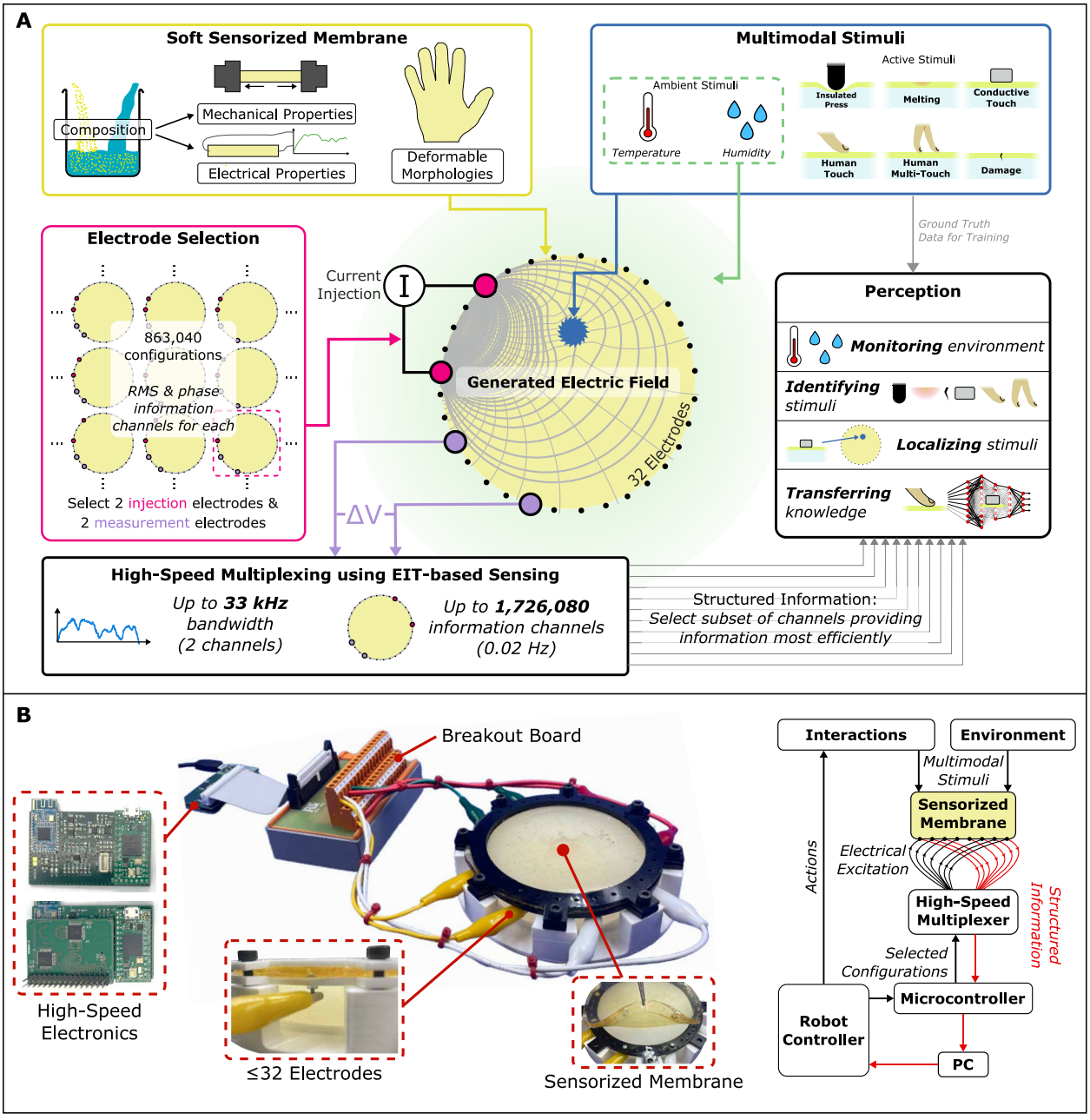

Fig. 1. Multimodal information structuring of a soft sensorized skin. (**A**) Multimodal stimuli are detected through the generation of an electric field across the skin using EIT hardware: The information that this returns can be structured through the skin's own composition and morphology and through the configuration of excitation electrodes. This work used a gelatin-based hydrogel as its soft membrane, because this can straightforwardly be cast into complex continuous shapes that contain no soft-rigid interfaces, such as a human-scale hand. By selectively exciting the membrane, structured information is output, which can be used to monitor environmental conditions, localize tactile stimuli, and explore the similarities and differences between multimodal stimuli. (**B**) The eight-electrode hydrogel membrane used for initial tests: High-speed electronics connected to the membrane's perimeter enable the comparison of all 1680 possible electrode configurations. A 10-cm circular membrane was fabricated, which was used to detect all the ambient and active stimuli presented in (A). In a fully implemented system, these data would be fed directly to the robot's controller.

the generated electric field measurements. By taking four-electrode measurements, we ensured that many channels were available for our data-driven analyses (1680 configurations compared with 56 for two-electrode measurements) and reduced the effect of contact impedances on our measurements.

We examined how six types of active stimuli affect the membrane's electric field: pressing with an insulated probe, touching with a human fingertip in one or multiple locations, touching with a conductive object, damage, and localized melting. Each of these stimuli is depicted in Fig. 2A, above their expected detection

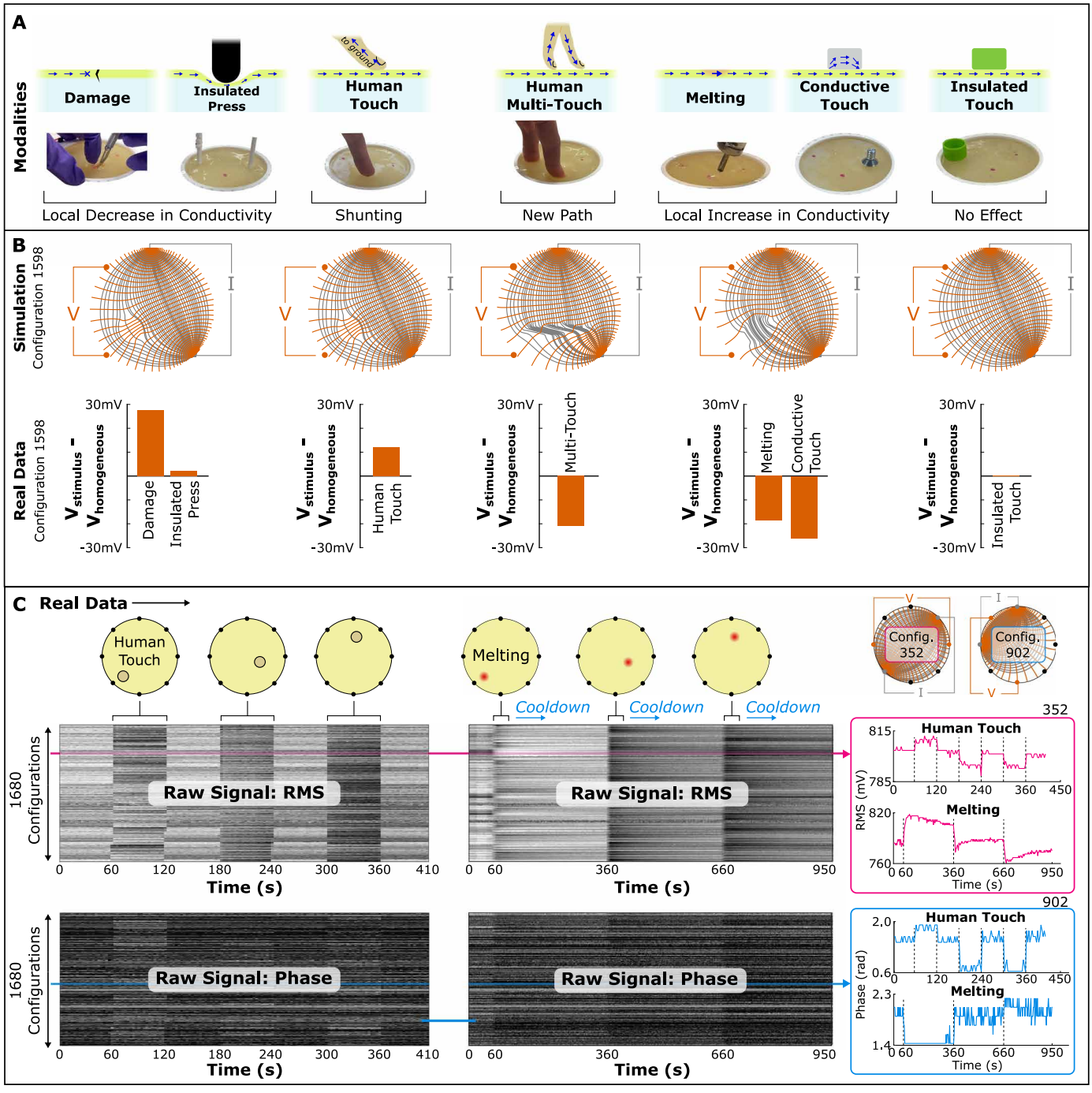

Fig. 2. Detecting multimodal stimuli using a generated electric field. (**A**) The seven modalities under consideration and their mechanisms of local conductivity impact on a soft hydrogel skin. Damage/insulated press and melting/conductive touch modalities are grouped in pairs given their similar mechanisms. (**B**) The effect of these mechanisms on one EIT-based tetrapolar electrode configuration around the eight-electrode circular skin. Simulations map the expected electric field in the presence of each stimulus, with bar graphs showing the measured responses when the seven modalities are applied to Fig. 1B's circular skin. (**C**) Raw responses from all 1680 electrode configurations for three differently located human touch and melting modalities. Each horizontal line plots the response of a single electrode configuration, normalized to fall within the range from 0 to 1. The raw time series responses of two configurations (numbered 352 and 902 in the 1680 full configuration sweep) are plotted over the same period.

mechanisms. A seventh stimulus—lightly touching with an insulated (plastic) object—was included as a baseline, because this was not expected to change the generated electric field. Figure 2B plots the idealized simulations of the stimuli's effects on one of the circular skin's electric fields (see the "Simulations" section in Materials and Methods). Electric current streamlines are plotted in gray, and the induced voltage equipotentials are plotted in orange.

Straining the hydrogel with an insulated press or cutting it with a scalpel both acted to locally decrease its conductivity, causing less current to flow through the stimulated region. For Fig. 2B's electrode configuration and stimulus location, the simulation predicts that this leads to an increase in the measured voltage (more equipotentials terminate between the measurement electrodes), which was also observed in the real data. Because damaging the membrane locally reduces its conductivity to zero, this had the largest magnitude (28 mV), whereas the response to the insulated press was only 2.2 mV. This was more than the insulated touch baseline in Fig. 2B's final column: As expected, this difference was negligible. Although both stimuli locally decreased the membrane's conductivity, differences in their spatial distributions could be identified by data-driven methods for modality classification: Damage cases will demonstrate very sharp transitions between conductivities, whereas a single press will cause a more gradual transition, resembling a 2D Gaussian curve. Instead of inferring these distributions from a reconstructed conductivity map, we looked for approaches in which such differences are identified directly, facilitating our method's scalability to more complex 3D skins.

Similarly, the melting and conductive touch modalities both caused a local increase in conductivity, which the simulation predicts will result in a decrease in the measured voltage. In our physical experiments, decreases of 19 and 26 mV, respectively, were measured, suggesting that the high conductivity of the steel bolt had the greatest effect. As before, we expected the different spatial distributions of these conductivity changes to be directly recognizable by an empirical approach. In addition, the two modalities behaved very differently temporally, which could be exploited by recurrent neural networks to provide additional information.

Last, the effect of human touch was considered, which we split into two cases: single-finger touches and multifinger touches. As described by Zhang *et al.* (*33*), single-finger touches draw a small amount of current to ground via the shunting effect, which cannot be represented with standard EIT models. Rather than modeling a current sink, Fig. 2B approximately modeled this as a local decrease in conductivity: A positive voltage change was observed, although its magnitude was difficult to predict. Conversely, touching the membrane with two fingers of the same hand provided a viable path for the current to flow, because human skin has a comparable resistance with the hydrogel (*52*). Again, this was not straightforwardly simulated; Fig. 2B's attempted local conductivity increase predicted little change in the measured voltage rather than the substantial decrease observed.

Decoupling multimodal information

So far, Fig. 2B has considered only the RMS response of 1 of the 1680 available electrode configurations. For each configuration, the measured signal's magnitude and phase shift both could be measured, giving a potential information throughput of 3360 information channels per frame. The information redundancies that these channels contain can be used to uniquely identify, localize, and transfer knowledge between various modalities without the need for stimuli-specific devices. In a fully implemented system, different configuration subsets would then be monitored on the basis of the desired stimuli, information rate, and required precision.

Some typical responses of the 3360 channels are shown in Fig. 2C. Each row plots the normalized 10-kHz signal against time from one of these channels as a finger was touched to three discrete locations on the physical membrane and removed between trials. Responses were visible in both the magnitude (RMS) and phase information channels. The overall response was noticeably different for each of the three locations: Using suitable information processing, localization is possible. The RMS and phase responses look very different for different modalities: Fig. 2C also plots the raw responses of the 3360 channels during localized melting of the same three locations. Rather than discrete events, melting was characterized by sharp steps when heat was applied, followed by a cooldown period in which responses began to drift back toward their starting point. These time-dependent behaviors are shown for two selected configurations on the right-hand side of Fig. 2C. At this stage, we did not know which configurations were best for predicting the type and location of each stimulus; we next explored how these measured responses can provide insights into the key similarities and differences between the modalities. Unless otherwise specified, tests were performed at 10 kHz. Figure S1 justifies the frequency selection, comparing the localized melting responses at three frequencies.

For the eight-electrode EIT skin, we could devise data-driven methods to select the information channels that provide maximum information about the tactile cues (see Supplementary Materials and Methods S4 for a simulation study on noise-free data for the same problem). We considered three objectives in data-driven configuration selection (Fig. 3): finding those that return the best information for each modality, those that return the best information regardless of modality, and those that are best for distinguishing between modalities. To do so, we individually applied seven modalities to the circular membrane: In addition to Fig. 2's modalities, we also applied presses with a human finger, which we consider as the combination of touch and insulated pressing mechanisms. Three arbitrarily chosen locations were used, marked A to C in Fig. 3A. The 1680 electrode configurations were recorded as all seven combinations of A, B, and C were applied, and their channel information was ranked using principal components analysis (PCA) to determine which most strongly influenced the variability of the response. (See the "Types of stimuli" in Materials and Methods. Additional insulated-press experiments with six fixed locations were repeated in fig. S13.) As depicted in Fig. 3B, each modality's PCA ranking was used to construct a characteristic "fingerprint" that we used as the basis of our configuration selection approach. The fingerprints were arranged such that a single row represents a fixed driving electrode pair, meaning that regular structures appear in the data—on the basis of the differences between the fingerprints, we visually gained an idea of their most important configurations. In the fingerprints, each modality's best configurations are represented by the darkest pixels: The top-ranked configuration for each is shown in Fig. 3C. The insulated touch was the only fingerprint in which regular structures do not appear, because the skin cannot respond to this modality. Hence, the insulated touch modality was not analyzed further. Human press, which combines the human touch and press modalities, appeared to be dominated by the human touch mechanism, with very similar fingerprint structures and the same top-ranked configuration.

To determine the best configurations regardless of modality, five of the fingerprints were averaged, giving the blue general fingerprint of Fig. 3C, in which darker pixels indicate better configurations. Given the similarities of the human press and human touch modalities, only human touch was used to construct this fingerprint to avoid skewing the result. The top four general configurations are

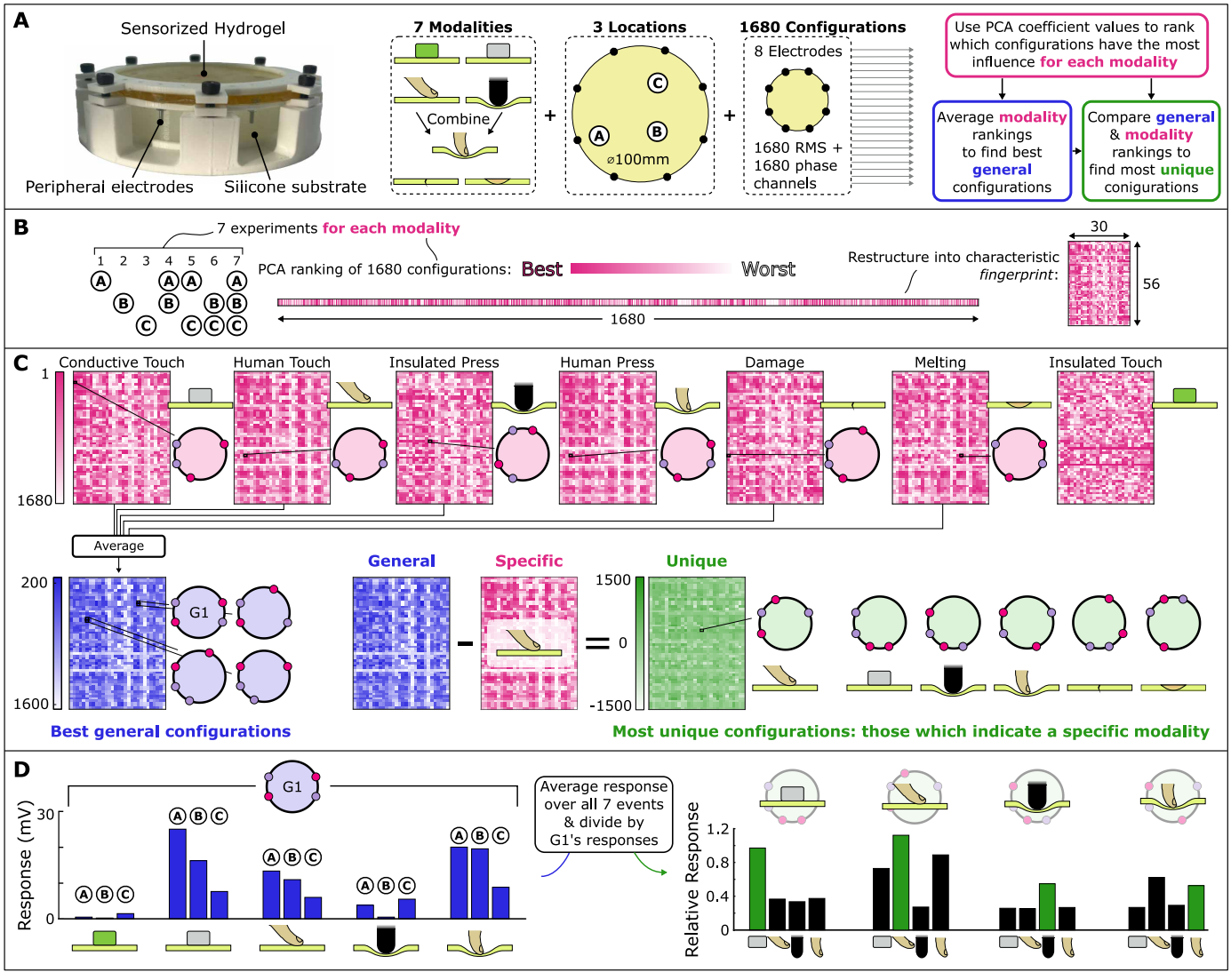

Fig. 3. Empirically identifying which configurations return the most valuable information to enable multimodal perception. (**A**) Seven modalities were used to stimulate the circular skin at three locations, whereas all 1680 electrode configurations were monitored. By ranking and comparing the responses, optimal configurations could be identified. (**B**) The generation of characteristic fingerprints for each modality based on the absolute PCA coefficients of the 1680 configurations' RMS magnitudes. Insulated touch does not return a structured fingerprint because of the membrane's inability to respond to this modality. (**C**) Using the fingerprints to identify the configurations that have the most influence for each modality, regardless of modality (referred to as the general case), and that generate a response most unique to each modality. (**D**) Response magnitudes using the best general configuration G1: These vary with modality and with location. Relative responses for four unique configurations are also plotted: As designed, these give the strongest response for their particular modality. Human touch and human press modalities appear to be most difficult to decouple.

shown, which provide the maximum information content about the stimuli.

Last, to identify unique configurations—those that respond in one modality more than the others—we considered the difference between the modality's own fingerprint and the general fingerprint. This approach is illustrated for a human touch in Fig. 3C: The darkest pixel of the green fingerprint represents its unique configuration, which was different from any of those already identified. This uniqueness was true for all configurations identified in Fig. 3C, representing the information channels, which could be used to identify particular modalities. From these identified channels, we can immediately see why a data-driven approach is most beneficial for decoupling multimodal signals, using high-density EIT to generate information.

The benefits of our fingerprinting approach are demonstrated in Fig. 3D, where the top-ranked general configuration (G1) was used to measure the responses of five modalities at the three locations. As expected, the insulated touch did not respond beyond experimental noise, whereas all others had responses that varied with location. The differences in magnitude between modalities are an indicator of how difficult each will be to analyze: Insulated presses gave a much weaker response than human or conductive touches. Response weakness could be partially addressed using the unique configurations: The final plot of Fig. 3D shows how the

average response at the three locations was changed from G1 by the unique configurations of four modalities. In three of the four cases, our fingerprinting approach identified configurations that maximized the signal from their particular modality. Only human press—which was not used in the general fingerprint—did not achieve this, instead maximizing the human touch change. This suggests that, although it will be difficult to distinguish between the two modalities, any localization results from one could be straightforwardly transferred to the other given their similar mechanisms. Transferring knowledge between the modalities with different mechanisms is more of a challenge: We considered an extension of our data-driven approach in Fig. 4.

Estimating multimodal information

To understand how we could differentiate between multiple stimuli, we first examined the similarity among all modality responses during Fig. 3B's seven experiments based on the coefficients of the first principal component (see Supplementary Materials and Methods S1). The results are plotted in Fig. 4A, where thicker connections indicate a higher similarity metric. As well as being similar to each other, both human modalities were very similar to the modalities that locally increase conductivity: conductive touch and melting. Conversely, both had minimal similarities to damage and insulated pressing, which locally decreased conductivity. We aimed to identify a modality that was sufficiently similar to all others, such that its further analysis provided insights into all modalities. Conductive touch was selected for this purpose; we first learned to localize the touch and then examined how this knowledge can be transferred (Fig. 4B).

For localization, Fig. 4C is based on the responses of the 3360 information channels to 1000 random placements of a steel nut onto the membrane by a robotic arm (movie S1). The information from the 3360 channels could be used to estimate the bolt's location using standard regression algorithms.

Rather than using all channels as the input to a feedforward neural network, we used only the N best configurations after all 1680 configurations were ranked using one of three methods. In an ideal system with no noise or nonlinearities, localization of a single stimulus could be performed with just five information channels (fig. S11). Because our physical system did not behave ideally, this ranking approach was used to ensure measurement efficiency for complex setups and could be straightforwardly expanded to noncircular membranes and skins. Two of the three ranking methods did not use any ground truth position data: "PCA" was the same ranking used to build Fig. 3's fingerprints, and the "environment" performed its ranking on the basis of how well the channels correlated to changes in humidity of the membrane over a 62-hour period (fig. S2). The final ranking method used the position data as the basis of a statistical F test (Supplementary Materials and Methods S1). All were compared with "adj/opp," which tested opposite and adjacent electrode positions (fig. S3). These electrode configurations were selected as a comparison given their widespread usage and practicality in sensorized robotic skins (*32*, *34*–*36*); we note that, in more traditional EIT setups, more suitable configuration approaches have been identified for the reconstruction of conductivity maps (*53*).

When the localization errors of a 10% test set were examined ($N = 1$ to 150) in Fig. 4C, all three ranking methods performed better than the adjacent/opposite configurations, with the F test ranking quickly converging to errors less than 10 mm. The improvement of the data-driven rankings stemmed in part from their ability to exploit asymmetries and nonlinearities in the physical material composition, multiplexer performance, and contact impedances (fig. S4). The distributions of errors over the membrane using the 20 best configurations are shown: Although PCA gave some regions of good localization, the adj/opp ranking had high errors distributed across the entire membrane. The F test gave a near-uniform distribution of low errors across the membrane's surface.

The F test ranking method provided a successful way of efficiently structuring the skin's output data, with its top 50 configurations resulting in better localization than 150 configurations of a standard sweep. We next used these top 50 configurations to map unseen modalities into a 2D plane where different stimuli could be visualized, built from the conductive touch data's first two principal components (Fig. 4D).

When the F test mapping was applied to the seven experiments of conductive touch, clusters were visible, corresponding to the untouched state, each individual location, and each multilocation combination. Using the vectors between each stimulus and the untouched state in Fig. 4D, each multilocation event could be reasonably predicted by superposing its individual locations (fig. S5). This observation suggests that each location elicits relatively independent responses from the structured channels—a behavior that we encouraged by statistically ranking the channels. Through finding configurations that identify specific regions of the membrane, we expected our structured output data to be generalizable to new modalities, which we tested in Fig. 4 (E to G). These figures used the same mapping, built from conductive touch's responses, to visualize the responses of three different modalities at the same locations: insulated press, human press, and melting. The scale was kept consistent: Larger vector magnitudes were due to greater raw responses. We have already seen in Fig. 3D that insulated presses have the smallest magnitude, but we then looked at the direction of its vectors (Fig. 4E), which were all in opposite directions from those of conductive touch (as shown directly in fig. S5). This shift in direction occured because the pressing caused a local decrease in conductivity, unlike conductive touch's local increase—knowing this mechanism, we could use the mapping to predict locations of the unseen modality, for both single- and multipress events—superposition also applies to this new modality. Further multipress predictions of up to six simultaneous insulated presses were explored in fig. S13, where this superposition was exploited by considering each location independently.

When mapping human press stimuli (Fig. 4F), there was a difference between single- and multipress modalities, as predicted by Fig. 2A's different mechanisms. The single-touch vectors of A, B, and C (corresponding to the locations marked in Fig. 3A) were in directions very similar to those of conductive touch. However, multipress produced a new path along which the current could flow and superposition did not apply—multipress produced much greater responses. Multipress events were still distinguishable, being separately clustered in the 2D mapping, but additional modeling layers would be required to accurately predict their locations.

The inverse relation between insulated press and conductive touch response vectors implies that melting, which locally increases conductivity, should result in response vectors aligning with those of conductive touch. This was the case: Fig. 4G shows a parametric plot with time as the membrane was heated and allowed to cool at A, B and C, each of which caused an outward motion in the same

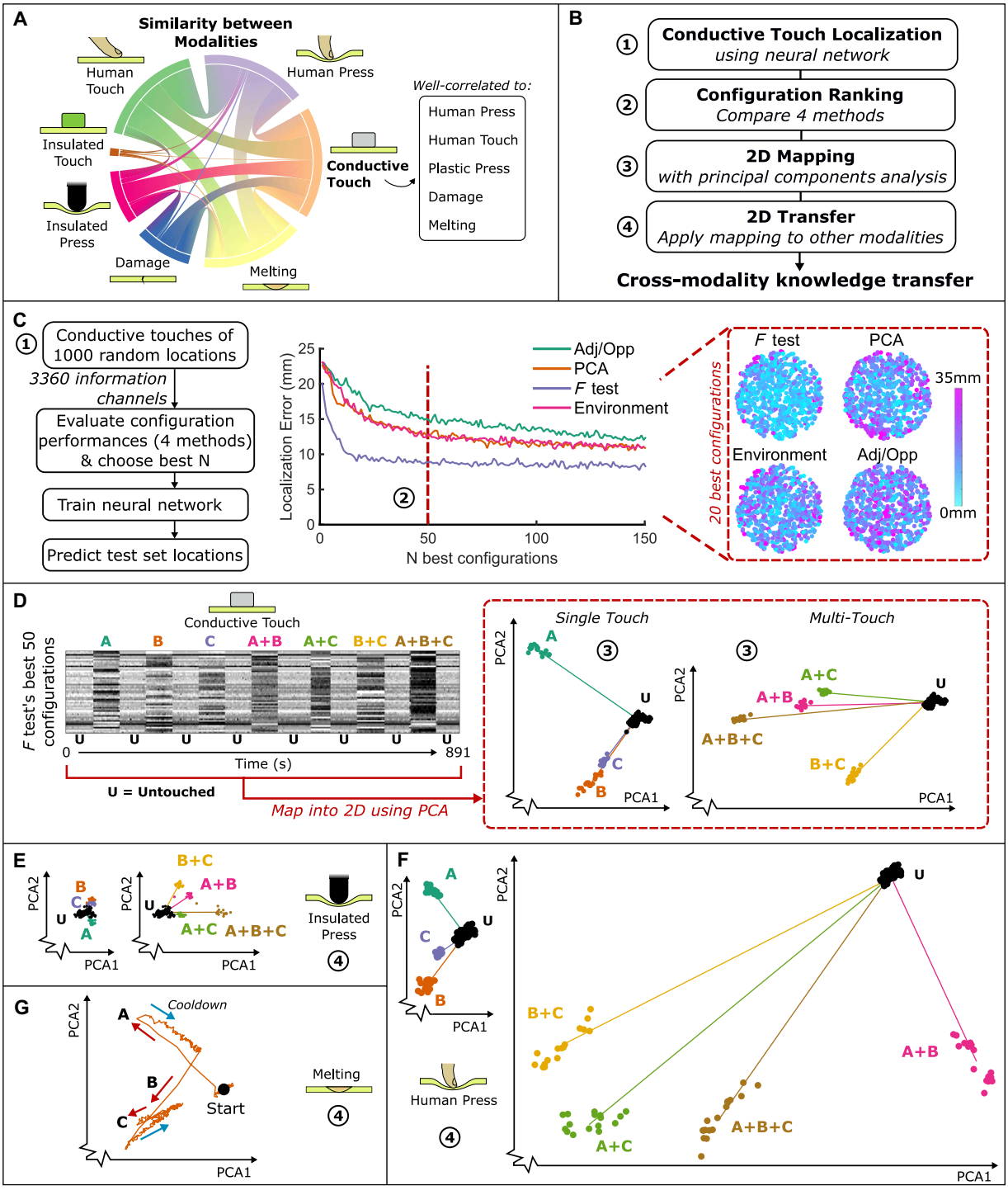

Fig. 4. Transferring localization knowledge to unseen modalities. (**A**) Similarities between the modalities based on the coefficients of their first principal component: Conductive touch was selected for transferability tests because of its high similarity to all other modalities. (**B**) The process of cross-modality knowledge transfer: A neural network was trained to localize conductive touch stimuli, and the key configurations were identified. These were used to visualize the responses of other modalities. (**C**) Four configuration-ranking methods are compared in structuring the input to a neural network that localizes 1000 conductive touches at random locations. When examining the convergence rates and distribution maps of localization errors on a 10% test set, statistical *F* test rankings performed best and were selected for cross-modality transfers. (**D**) The *F* test's 50 best configurations were used to map the responses into a 2D plane through PCA where different stimulus locations can be visualized. Multitouch vectors can be superposed from single-touch vectors. (**E**) The same mapping was applied to insulated press, which gave smaller response vectors in the opposite direction. (**F**) The mapping was applied to human presses, which behaved similarly for single locations and responded very strongly to multilocation presses because of Fig. 2A's new mechanism. (**G**) The mapping was applied to the localized melting time series to produce a parametric plot (movie S1), with response vectors in the same direction as conductive touch because of their shared response mechanism.

direction as that of the conductive touch (movie S1). These transferability findings (illustrated fully in fig. S5) indicate that, by knowing the mechanism by which a sensing modality affects the electric field of an asymmetric membrane, the results from training on only one modality can be used to make sensible predictions and the locations of totally unseen modalities. Coupled with knowledge of the unique configurations (Fig. 3C), this transferability provides a data-driven pipeline for multimodal sensing in the skin: Unique configurations are monitored to detect and classify a particular stimulus, the location of which is then predicted using conductive touch's trained model. In addition, we know from Hardman *et al.* (*52*) that environmental conditions can be straightforwardly monitored using just a handful of configurations, facilitating a skin that not only responds to multiple stimuli but also can track the conditions in which it is doing so. The data-driven nature of our approach means that it could be applied to setups for which analytic approaches would ordinarily struggle: 3D skins and anisotropic conductivities.

A single-layer sensorized soft hand

To demonstrate how combining information structuring with high-density EIT can enable highly functional robotic skins, we moved from the 2D circular membrane to a more complex 3D morphology: a full-size hollow 3D hand cast entirely from the soft sensorized hydrogel. Figure 5 presents the key components of its design; with 32 electrodes arranged around its wrist, there were 863,040 available electrode configurations and 1,726,080 available information channels. These configurations were used to generate electric fields across the hand, the monitoring of which enabled multimodal sensing through the mechanisms introduced in Fig. 2. Despite the complex 3D shape, information-rich subsets of the 863,040 electrode configurations could be identified with our approach, such that stimuli could be recognized and interpreted with an efficient balance of information rate and content.

A new proprioceptive response was also introduced: Strains from the bending of the fingers caused conductivity changes that could be detected in the raw signals. Unlike previous skins for robotic hands, the entire surface area of our design contained no soft/rigid interfaces, because electrodes were introduced only at the wrist. The free surface made the skin fully stretchable, fully continuous, and free to capture multimodal interactions occurring anywhere over its surface. Because the hand was made from just one material, there was no risk of delamination. Local damage to the surface did not affect device architecture, and the material itself exhibited healing properties (*52*), making the artificial skin highly robust.

Figure 5B depicts the hand's fabrication process: A silicone mold was cast around a 3D-printed positive before a smaller "inner positive" was inserted, a flexible sleeve containing conductive threads was added, and the hydrogel was cast. After removal from the mold, the inner positive was removed through the empty cross section of the wrist to leave a soft hollow membrane, which was firmly secured into a base through which the 32 electrodes were wired. More details can be found in fig. S7 and in Supplementary Materials and Methods S3.

The hand immediately responded to human touch, conductive touch, and finger bending (figs. S8 to S10). We focused on the information structuring that is required for human-robot interactivity (localizing light human touches over the skin's surface) and for environmental monitoring (of temperature and humidity). Given the electrode positions, any generated electric fields will be weakest at the skin's fingertips. To account for this distribution, our data-driven ranking approach skewed toward selecting configurations that provide localization information toward these areas, rather than only near the base. Alternatively, the hydrogel's composition could be locally varied to provide material-level information structuring, increasing the conductivity of channels that encourage current flow toward the fingertips (*36*). This approach was briefly explored in fig. S6.

In Fig. 6, we demonstrate how our data-driven ranking methods can perform human touch detection on this complex 3D surface. First, all 1,726,080 channels were monitored as the hand was touched in three locations (Fig. 6A). Even touches at the fingertip, furthest from the electrodes, could be seen in the raw data. From these representative responses, the Fig. 3's approach was used to generate an 870-configuration-by-992-configuration fingerprint from which the 2784 best-ranked configurations were selected.

To characterize our method's localization capabilities, 1080 random locations over the hand's 38,000-mm^2 area were touched, whereas 11,136 channels were monitored: the 2784 selected fingerprinting configurations and the 2784 adjacent/opposite EIT configurations. By prefiltering 5568 of the 863,040 available configurations, we balanced between a dataset that could be collected efficiently (11,136 channels every 6.5 s; table S1) and collecting sufficiently structured data to run a more thorough ranking for successful localization. Before any further channel reduction was done, the method of weighted activation maps [WAMs; presented in (*49*)] was used to predict the locations of a 10% test set, given N channels. Figure 6B plots the resulting localization errors ("without ranking"), which converged very slowly, with localization errors averaging more than 40 mm even when using 500 random channels. However, when the F test ranking method was introduced to structure the standard configurations, localization errors fell below 30 mm using just 40 channels, because our data-driven search identified those that were capable of providing the most beneficial information despite the presence of measurement noise (fig. S12).

With more configurations available to structure, the localization became even more accurate and efficient: Fig. 6B's rightmost graph plots the $N = 500$ localization errors. Using the F test ranking, localization was possible to 24.7 mm over the 380-cm^2 area of the hand (movie S2). To examine how this was achieved, Fig. 6B also demonstrates the activation maps of the 10 best configurations: their average responses to 1080 touches over the area of the hand. Using only these 10 signals, localization errors below 40 mm could be achieved. In each, a particular area of the hand responded most strongly to the light touches; by combining multiple such configurations, the WAM method could efficiently predict the touch location. Localizing the touch with so few channels enabled higher frame rates during data collection (up to 3.3 kHz for 10 channels in table S1), promising the analysis of increasingly dynamic data. In addition, this localization of human touch was achieved with fewer than 496 channels—the maximum number of independent channels predicted by N-port theory (*46*)—ensuring that additional information is available for multimodal predictions.

For example, the soft 3D hand could also monitor and predict its environmental conditions, as shown in Fig. 6C and movie S2. The responses of the 5568 configurations were recorded over a 100-hour period in the laboratory. During this time, the environmental temperature and humidity moved between 19° and 25°C and 38 and 72%, respectively. By ranking the responses using the Fig. 4's F test

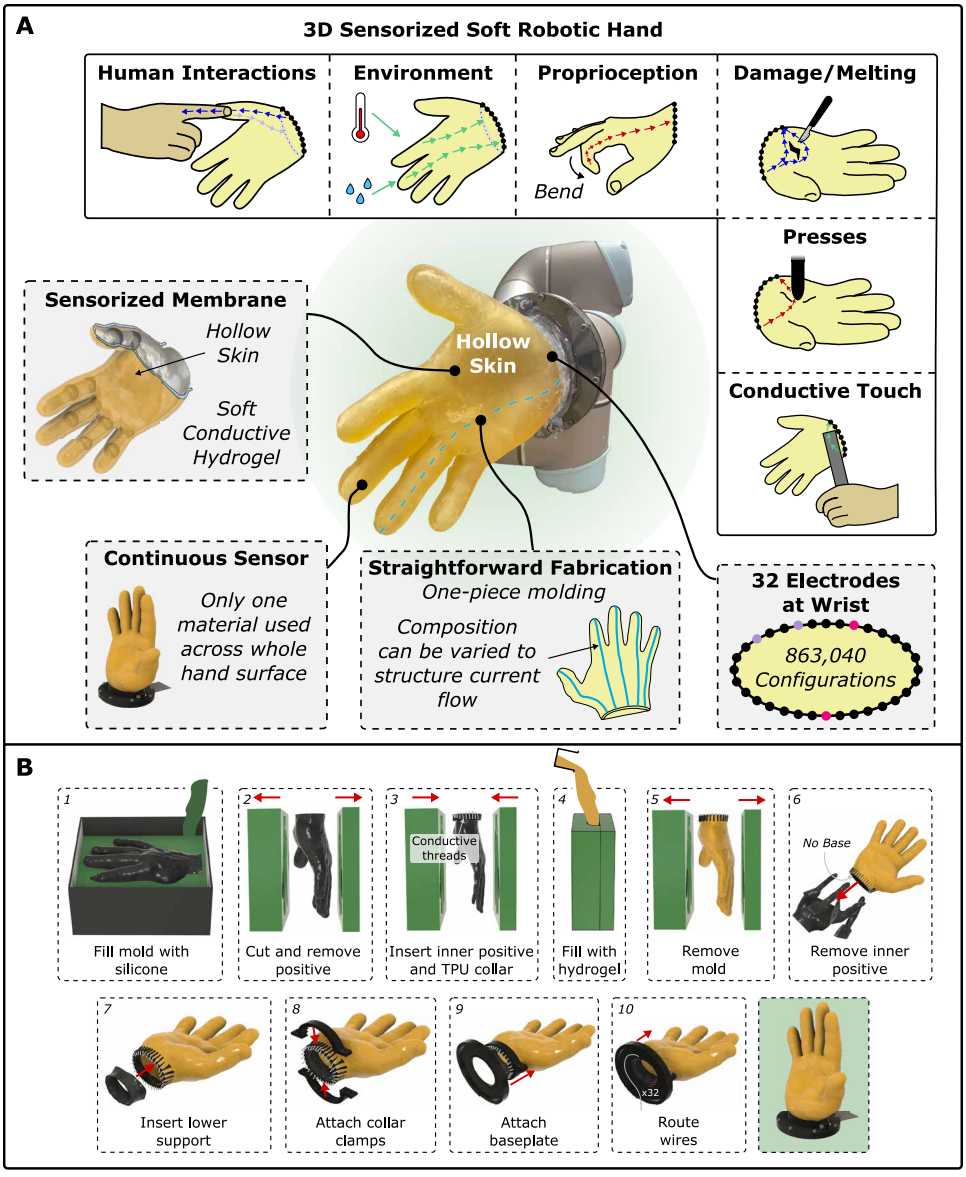

Fig. 5. Application to 3D skins: Design of a hollow hand. (**A**) A hollow skin was cast from the sensorized hydrogel, with 32 electrodes positioned around its wrist. The hand's entire surface is continuous and contains no soft/rigid interfaces. A total of 863,040 electrode configurations are available to detect multimodal stimuli. In addition to the modalities already considered, a new proprioceptive response is possible when the fingers bend. (**B**) Fabrication steps of the skin. Positive inserts and a thermoplastic polyurethane (TPU) collar were used to create the hollow membrane, with all 32 electrodes being routed into a ribbon cable at the hand's base to connect to EIT hardware. A full description of the process is given in the Supplementary Materials.

approach, 50 signals were sufficient to train a neural network to accurately predict environmental temperature and humidity in a 10% test set, as shown in Fig. 6C. These fluctuations caused changes in the hydrogel's conductivity, which affected the measurements of the skin's generated field. Subsequently, a global drift could be seen: Fig. 6A plots the mean RMS response of all 863,040 configurations averaged over 870 groups of 992 channels. Although some channels were noisier than others, this drift corresponds to ground truth measurements of the actual environmental conditions. In addition, tactile data could be recorded and predicted during this same period: The gray bars indicate a period over which 250 random locations were touched and localized with an average error of 26.3 mm. Figure 6D shows the distribution of localization errors: The structured configurations kept this low over the majority of the hand, with higher errors mostly at the fingertips. In Fig. 6E, the WAM predictions of eight consecutive test set touches are plotted, where brighter yellow regions are those predicted to be most likely to contain the stimulus. With an average error of 25.1 mm, these provide a representation of typical predictions over the 1080 recorded touches. In three cases, the front/back classification was predicted incorrectly. These were cases in which the stimulus was very close to the perimeter, such that the front and back touches were physically very close. More examples are shown in movie S2. In addition, an initial application of our channel ranking plus the WAM approach to further multimodal predictions is presented in fig. S14. Human multitouch predictions across a new 32-electrode 3D hand were made at the same time as local temperature predictions at the base of its thumb. Channel ranking was used to treat front predictions, back predictions, and temperature predictions independently. Results are shown further in fig. S15 and movie S3, and full details are given in Supplementary Materials and Methods S5.

DISCUSSION

Current multimodal tactile sensing technologies are developed from a bottom-up approach, designing modality-specific devices that are combined using complex fabrication techniques and smart materials to make them flexible and scalable. This approach makes them difficult to manufacture, expensive, prone to delamination and damage, and susceptible to interference. Our results demonstrate a top-down approach for the multimodal sensorization of complex skins: Using our information-structuring framework, we were able to localize light touches over the surface of a homogeneous hand with electrodes positioned only around its wrist. Thirty-two electrodes provide more than 1.7 million information channels across the sensorized material, containing data from multimodal interactions and environmental conditions with inbuilt redundancies that ensure robustness. This abundance of data presents challenges in the processing of sensory information that stimuli-specific sensing devices do not have, but our architecture provides more flexibility in the design, fabrication, and scale. To

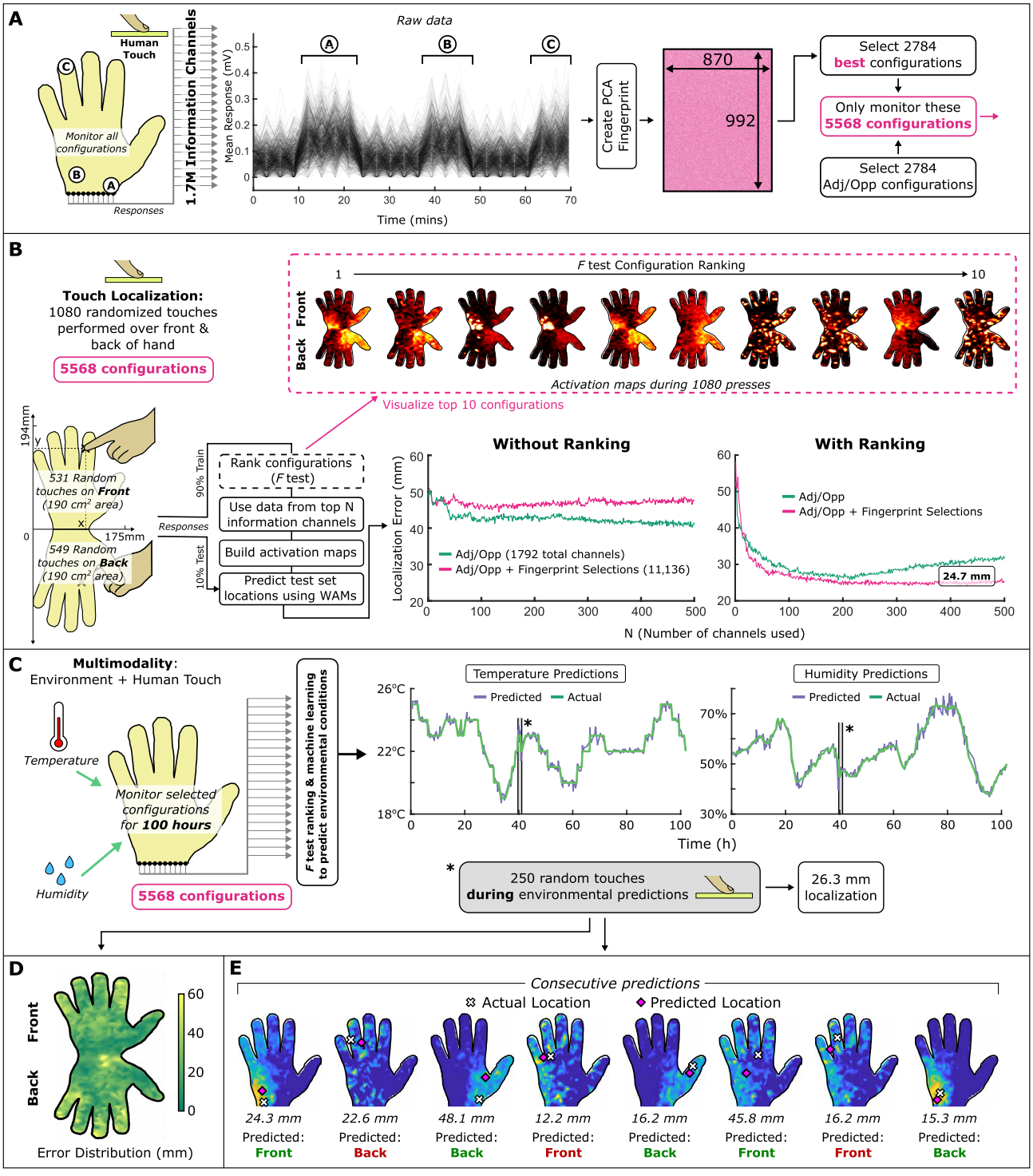

Fig. 6. Structuring information to predict multimodal stimuli in the 3D hand. (**A**) Even with the electrodes at the wrist, tactile responses were still seen in the setup's 1,726,080 information channels. Fingerprinting was used to select which should be monitored. (**B**) Using *F* test ranking to improve the efficiency of tactile localization. A total of 1080 randomized light touches over the front and back of the hand were predicted using the WAM method: Using *N* channels, the average localization errors of a 10% test set were plotted. Activation maps of the 10 top-ranked configurations are shown, which respond to touches in different areas of the hand. (**C**) Using the *F* test to select the channels, accurate predictions of environmental temperature and humidity for a 10% test set can be learned by a neural network while touches are taking place. (**D**) Error distributions over the front and back of the hand. (**E**) Eight test set predictions from the multimodal measurements.

address the challenge of efficiently obtaining relevant state information from these numerous channels, we present a multilevel information structuring method. Using passive information from the environment with the combination of statistical techniques, modality-relevant information channels can be quickly identified. This is followed by standard nonlinear regression for state estimation. We demonstrate how the information structuring of such channels can be used to identify and process multimodal stimuli, increase the efficiency of tactile localization, and transfer knowledge between modalities. Using this approach, we highlight a promising route for increasing the complexity of 3D multimodal skins with peripheral electrodes for direct application to wearable sensors, robots, and prosthetic devices.

So far, we have demonstrated our sensing strategy using a homogeneous material, showing the benefits of our information-structuring approach to the multimodal sensing of complex shapes. Even with the *F* test ranking, the homogeneous material properties led to decreased sensitivities at the hand's fingertips, furthest from the electrodes. As EIT technologies continue to be developed for single-layer 3D shapes, sensitivity distributions can be influenced in two ways: electrode repositioning and material anisotropies. Repositioning electrodes to locations where they will generate stronger signals makes the areas more sensitive but restricts motions and physical interactions and increases delamination risk. Conversely, the introduction of conductivity anisotropies (as explored in fig. S6) into the material would serve to bias the direction of current flow while keeping electrodes at convenient locations. With hydrogels, this could be implemented through local changes in composition; a skin's initial conductivity distribution and electrode location could be optimized in simulation before fabrication. Still, without first-principle models, it is not possible to predict the properties of our sensory skin. This makes specification-driven design and design optimization challenging. Data-driven design optimization techniques have to be used in this case (*54*, *55*), and we expect that a realistic design pipeline of our approach would couple the faster iterations of simulated models with the empirical data of physical modeling.

Figure 1 introduced the hydrogel composition used as the basis of the sensorized membranes throughout this work. Its responsiveness to particular stimuli determined the range of multimodal properties that we were able to demonstrate; those capable of influencing a generated electric field can be monitored through our approach. Similarly, the selection of different conductive and functional materials could be used to introduce new modalities, including magnetic, chemical, and light sensitivities. For a material's complete system integration, these electrical properties must be considered alongside its mechanical, fabrication, and robustness characteristics. Hydrogels are typically associated with drying out over short time periods: Although the composition used here can remain stable over multiple months (*52*), its mechanical properties and physical dimensions fluctuate within a typical range of environmental temperatures and humidities, and it has a relatively low maximum operating temperature. The effects of humidity can be lessened through the introduction of a nonpermeable covering, although this moves into a multilayer system in which the chances of delamination and adhesion issues are greatly increased. Instead, for more stable implementations, conductive elastomers—such as the carbon-infused silicones popular in soft robotic systems—could be explored.

By using a single-layer skin, our hand was stretchable and could not delaminate. Its weakest points were at the only remaining soft-rigid connections: the wrist. As described in Supplementary Text, clamped connections, conductive thread, and adhesives of intermediary stiffness were used to ensure that this interface was as robust as possible. Subsequent iterations and improvements in flexible electronic adhesion could look to integrate more flexibility into these connection points, transforming them into safer soft-soft interfaces.

Additional future work includes the exploration of methods for the transferability of learned channel rankings between different sensors. We began our approach by neglecting reciprocity assumptions within the system in favor of a data-driven approach: Once any hardware nonlinearities have been learned, then this step may not be necessary, improving training efficiency. Once efficient frameworks have been developed, a promising direction of development is the execution of high-level touch-driven tasks for robotic manipulation using sensorized skin. Because the soft skin is hollow and stretchable, we can easily wrap existing robotic manipulators with minimal effects on the robot's motion. Raw data from the EIT channels after the first stage of information structuring or fully processed multimodal information can be used as state observations to close the loop for contact-rich tasks (*56*).

MATERIALS AND METHODS

Electrically conductive membrane

The electrically conductive skin was cast from a gelatin-based hydrogel as described by Hardman *et al.* (*52*). Gelatin powder (MM Ingredients) was mixed with water, glycerol (Themo Fisher Scientific), and citric acid monohydrate (Themo Fisher Scientific) at a mass ratio of 1:1.5:1.5:0.2 and left to homogenize for 48 hours in an oven at 50°C, during which salt (Sainsburys) was added at a mass ratio of 1:0.1 to the gelatin powder. To create the circular membrane from Figs. 1 to 4, this mixture was poured into a laser-cut acrylic mold of 110-mm diameter and 3-mm thickness. Once solidified, the membrane was clamped between two laser-cut acrylic frames, pressing eight equally stainless steel M2.5 bolts into its surface at a 100-mm diameter to function as the electrodes. This setup was bolted onto a 3D-printed support, which held a 90-mm cylinder of Ecoflex 00-20 silicone underneath the exposed hydrogel surface. The resulting setup is shown in Fig. 3A: Any presses of the skin also pressed into the silicone substrate. Figure 1 shows the interface between the electrodes and the high-speed electronics: One crocodile clip was clamped to each of the eight electrodes, which joined to a 32-pin ribbon cable via an insulation displacement contact (IDC) breakout board. Figures 3 and 4's experiments were performed at environmental conditions of 55% humidity and 19°C. Full details of the hollow hand's casting process and electrode integration are provided in Supplementary Materials and Methods S3, and computer-aided design (CAD) files are provided in the code repository.

Electronics

Throughout this work, electric fields were generated and measured using Zhu *et al.*'s open-source EIT-kit motherboard (shown in Fig. 1B), designed for human health and motion monitoring via EIT (*57*). To match the impedance of the hydrogel, four resistor values were changed from the original design: R7, R8, R21, and R22 were set to either 100 ohms (2D membrane) or 50 ohms (3D hand). The Teensy 4.0 microcontroller that controlled this board was programmed through the Arduino integrated development environment (IDE), and measurements were returned to a serially

connected laptop through a universal serial bus (USB) cable. Voltage and current gains were set manually for each setup, as were each configuration's electrode locations via its multiplexer. Table S1 details the frequencies and speeds used throughout this work: The fields from injection frequencies between 10 and 100 kHz were measured using the onboard 20-MHz analog-to-digital converter (ADC). By varying the controller's averaging factor and wait times, single measurements were returned at a rate of up to 33 kHz. Specific rates were selected for each experiment to compromise between measurement speed and noise reduction.

Simulations

Figure 2 (B and C)'s electric field simulations were generated using EIDORS's in-built forward solver (*58*), implemented in MATLAB 2023a. A circular model with eight electrodes and low vertex density was constructed, with identification string d2d1c. Stimulation patterns were input manually, and the field was visualized using MATLAB's streamline() and contour() functions for current and voltage, respectively. To simulate the insulated touch's effect, a homogeneous membrane was assumed, whereas other modalities were represented by changing the conductivity of a circle one-fifth the diameter of the membrane. The "new path" mechanism was represented using a variable-conductivity ellipse. In Fig. 2B, current was injected at electrodes 5 and 8 while being measured at electrodes 2 and 4. This corresponds to configuration 1598, which was selected such that stimuli at point A resulted in a visible effect to the generated field. In configurations 352 and 902, this order was 2, 6, 3, and 7 and 3, 5, 1, and 4, respectively. Code is provided with this manuscript.

Types of stimuli

Figure 3's control stimulus (insulated touch) was applied by placing 1.5-g polypropylene twist caps at locations A, B, C, A plus B, A plus C, B plus C, and A plus B plus C in turn for 1 min, with 1-min gaps between each stimulus. Insulated press, conductive touch, human touch, and human press followed the same order and timings (photos of each are given in Fig. 3A), with conductive touch using a 6.5-g stainless steel bolt, human touch using the fingers of the experimenter's left hand to gently contact the membrane, human press using the fingers of the experimenter's left hand to depress the membrane by ~10 mm, and insulated press using 5-mm-diameter polylactic acid (PLA) probes attached to a UR5 robotic arm to depress the membrane by 8 mm. For the melting stimuli, a rework station's heat gun, set to 200°C, was brought close to locations A, B, and C in turn, each for 15 s with 5-min intervals for cooling. During damage, the experimenter wore nitrile gloves and used a 10A scalpel blade to cut the membrane at locations A, B, and C, holding each cut open for 1 min and then releasing for 1 min before cutting the next. During all modalities, RMS and phase information from all 1680 channels at 10, 50, and 100 kHz were monitored at a frame rate of 0.33 Hz (table S1). The 10-kHz recordings were used in subsequent analysis.

Processing and localization

Information processing and stimulus localizations were implemented using MATLAB 2023a. Supplementary Materials and Methods S1 provides specific details behind the creation of Figs. 3 (B to D) and 4 (A to C and E to G). Supplementary Materials and Methods S2 provides specific details behind the localization methods of Figs. 4D and 6 (A to E).

Statistical analysis

Figures 2, 3, 4, and 6 present data from individual experiments, using a large number of channels and randomized locations, which are reported in the captions. Reported localization errors throughout the manuscript are the mean errors of an isolated test set (10% unless otherwise stated). Details of specific implementations are provided in Supplementary Materials and Methods and in the attached code.

Supplementary Materials

The PDF file includes:

Tables S1 and S2
Figs. S1 to S15
Materials and Methods S1 to S5
Legends for movies S1 to S3
References (*58*–*65*)

Other Supplementary Material for this manuscript includes the following:

Movies S1 to S3

REFERENCES AND NOTES

1. R. S. Johansson, J. R. Flanagan, Coding and use of tactile signals from the fingertips in object manipulation tasks. *Nat. Rev. Neurosci.* **10**, 345–359 (2009).
2. R. S. Dahiya, in *Robotic Tactile Sensing: Technologies and System*, R. S. Dahiya, M. Valle, Eds. (Springer, 2013), pp. 81–101.
3. J. A. Rogers, T. Someya, Y. Huang, Materials and mechanics for stretchable electronics. *Science* **327**, 1603–1607 (2010).
4. B. Shih, D. Shah, J. Li, T. G. Thuruthel, Y.-L. Park, F. Iida, Z. Bao, R. Kramer-Bottiglio, M. T. Tolley, Electronic skins and machine learning for intelligent soft robots. *Sci. Robot.* **5**, eaaz9239 (2020).
5. S. Zhang, Z. Chen, Y. Gao, W. Wan, J. Shan, H. Xue, F. Sun, Y. Yang, B. Fang, Hardware technology of vision-based tactile sensor: A review. *IEEE Sensors J.* **22**, 21410–21427 (2022).
6. Y.-L. Park, B.-R. Chen, R. J. Wood, Design and fabrication of soft artificial skin using embedded microchannels and liquid conductors. *IEEE Sensors J.* **12**, 2711–2718 (2012).
7. O. Shorthose, A. Albini, L. He, P. Maiolino, Design of a 3D-printed soft robotic hand with integrated distributed tactile sensing. *IEEE Robot. Autom. Lett.* **7**, 3945–3952 (2022).
8. K. Gilday, T. George-Thuruthel, F. Iida, Predictive learning of error recovery with a sensorized passivity-based soft anthropomorphic hand. *Adv. Intell. Syst.* **5**, 2200390 (2023).
9. Y.-L. Park, C. Majidi, R. Kramer, P. Bérard, R. J. Wood, Hyperelastic pressure sensing with a liquid-embedded elastomer. *J. Micromech. Microeng.* **20**, 125029 (2010).
10. S. Russo, T. Ranzani, H. Liu, S. Nefti-Meziani, K. Althoefer, A. Menciassi, Soft and stretchable sensor using biocompatible electrodes and liquid for medical applications. *Soft Robot.* **2**, 146–154 (2015).
11. H. Yousef, M. Boukallel, K. Althoefer, Tactile sensing for dexterous in-hand manipulation in robotics—A review. *Sens. Actuators A Phys.* **167**, 171–187 (2011).
12. J. Tu, M. Wang, W. Li, J. Su, Y. Li, Z. Lv, H. Li, X. Feng, X. Chen, Electronic skins with multimodal sensing and perception. *Soft Sci.* **3**, 25 (2023).
13. Z. Yuan, S.-T. Han, W. Gao, C. Pan, Flexible and stretchable strategies for electronic skins: Materials, structure, and integration. *ACS Appl. Electron. Mater.* **4**, 1–26 (2022).
14. M. Weigel, T. Lu, G. Bailly, A. Oulasvirta, C. Majidi, J. Steimle, "iSkin: Flexible, stretchable and visually customizable on-body touch sensors for mobile computing," in *CHI '15: Proceedings of the 33rd Annual ACM Conference on Human Factors in Computing Systems* (Association for Computing Machinery, 2015), pp. 2991–3000.
15. M. Teyssier, G. Bailly, C. Pelachaud, E. Lecolinet, A. Conn, A. Roudaut, "Skin-on interfaces: A bio-driven approach for artificial skin design to cover interactive devices," in *UIST '19: Proceedings of the 32nd Annual ACM Symposium on User Interface Software and Technology* (Association for Computing Machinery, 2019), pp. 307–322.
16. S. Harada, W. Honda, T. Arie, S. Akita, K. Takei, Fully printed, highly sensitive multifunctional artificial electronic whisker arrays integrated with strain and temperature sensors. *ACS Nano* **8**, 3921–3927 (2014).
17. Y. Wang, D. Liu, Y. Zhang, L. Fan, Q. Ren, S. Ma, M. Zhang, Stretchable temperature-responsive multimodal neuromorphic electronic skin with spontaneous synaptic plasticity recovery. *ACS Nano* **16**, 8283–8293 (2022).
18. J. W. Booth, D. Shah, J. C. Case, E. L. White, M. C. Yuen, O. Cyr-Choiniere, R. Kramer-Bottiglio, Omniskins: Robotic skins that turn inanimate objects into multifunctional robots. *Sci. Robot.* **3**, eaat1853 (2018).

19. T. Mukai, M. Onishi, T. Odashima, S. Hirano, Z. Luo, Development of the tactile sensor system of a human-interactive robot "RI-MAN". *IEEE Trans. Robot.* **24**, 505–512 (2008).
20. A. Schmitz, M. Maggiali, L. Natale, B. Bonino, G. Metta, "A tactile sensor for the fingertips of the humanoid robot iCub," in *2010 IEEE/RSJ International Conference on Intelligent Robots and Systems* (IEEE, 2010), pp. 2212–2217.
21. T. Yoshikai, H. Fukushima, M. Hayashi, M. Inaba, "Development of soft stretchable knit sensor for humanoids' whole-body tactile sensibility," in *2009 9th IEEE-RAS International Conference on Humanoid Robots* (IEEE, 2009), pp. 624–631.
22. P. Mittendorfer, G. Cheng, Humanoid multimodal tactile-sensing modules. *IEEE Trans. Robot.* **27**, 401–410 (2011).
23. P. Maiolino, A. Ascia, M. Maggiali, L. Natale, G. Cannata, G. Metta, "Large scale capacitive skin for robots," in *Smart Actuation and Sensing Systems*, G. Berselli, R. Vertechy, G. Vassura, Eds. (IntechOpen, 2012), chap. 8.
24. L. Chen, X. Chang, H. Wang, J. Chen, Y. Zhu, Stretchable and transparent multimodal electronic-skin sensors in detecting strain, temperature, and humidity. *Nano Energy* **96**, 107077 (2022).
25. A. Georgopoulou, D. Hardman, T. G. Thuruthel, F. Iida, F. Clemens, Sensorized skin with biomimetic tactility features based on artificial cross-talk of bimodal resistive sensory inputs. *Adv. Sci.* **10**, e2301590 (2023).
26. Z. Yuan, G. Shen, Materials and device architecture towards a multimodal electronic skin. *Mater. Today* **64**, 165–179 (2023).
27. S. Shimadera, K. Kitagawa, K. Sagehashi, Y. Miyajima, T. Niiyama, S. Sunada, Speckle-based high-resolution multimodal soft sensing. *Sci. Rep.* **12**, 13096 (2022).
28. T. G. Thuruthel, J. Hughes, A. Georgopoulou, F. Clemens, F. Iida, Using redundant and disjoint time-variant soft robotic sensors for accurate static state estimation. *IEEE Robot. Autom. Lett.* **6**, 2099–2105 (2021).
29. I. Andrussow, H. Sun, K. J. Kuchenbecker, G. Martius, Minsight: A fingertip-sized vision-based tactile sensor for robotic manipulation. *Adv. Intell. Syst.* **5**, 2300042 (2023).
30. B. Ward-Cherrier, N. Pestell, L. Cramphorn, B. Winstone, M. E. Giannaccini, J. Rossiter, N. F. Lepora, The tactip family: Soft optical tactile sensors with 3D-printed biomimetic morphologies. *Soft Robot.* **5**, 216–227 (2018).
31. K. Park, H. Yuk, M. Yang, J. Cho, H. Lee, J. Kim, A biomimetic elastomeric robot skin using electrical impedance and acoustic tomography for tactile sensing. *Sci. Robot.* **7**, eabm7187 (2022).
32. H. Alirezaei, A. Nagakubo, Y. Kuniyoshi, "A highly stretchable tactile distribution sensor for smooth surfaced humanoids," in *2007 7th IEEE-RAS International Conference on Humanoid Robots* (IEEE, 2007), pp. 167–173.
33. Y. Zhang, G. Laput, C. Harrison, "Electrick: Low-cost touch sensing using electric field tomography," in *CHI '17: Proceedings of the 2017 CHI Conference on Human Factors in Computing Systems* (Association for Computing Machinery, 2017), pp. 1–14.
34. K. Liu, Y. Wu, S. Wang, H. Wang, H. Chen, B. Chen, J. Yao, Artificial sensitive skin for robotics based on electrical impedance tomography. *Adv. Intell. Syst.* **2**, 1900161 (2020).
35. X. Duan, S. Taurand, M. Soleimani, Artificial skin through super-sensing method and electrical impedance data from conductive fabric with aid of deep learning. *Sci. Rep.* **9**, 8831 (2019).
36. A. Costa Cornellà, D. Hardman, L. Costi, J. Brancart, G. Van Assche, F. Iida, Variable sensitivity multimaterial robotic e-skin combining electronic and ionic conductivity using electrical impedance tomography. *Sci. Rep.* **13**, 20004 (2023).
37. H. Lee, K. Park, J. Kim, K. J. Kuchenbecker, "Internal array electrodes improve the spatial resolution of soft tactile sensors based on electrical resistance tomography," in *2019 International Conference on Robotics and Automation (ICRA)* (IEEE, 2019), pp. 5411–5417.
38. M. Cheney, D. Isaacson, J. C. Newell, Electrical impedance tomography. *SIAM Rev.* **41**, 85–101 (1999).
39. K. Park, H. Lee, K. J. Kuchenbecker, J. Kim, Adaptive optimal measurement algorithm for ERT-based large-area tactile sensors. *IEEE/ASME Trans. Mechatron.* **27**, 304–314 (2022).
40. S. Wang, Z. Sun, Hydrogel and machine learning for soft robots' sensing and signal processing: A review. *J. Bionics Eng.* **20**, 845–857 (2023).
41. A. Adler, P. O. Gaggero, Y. Maimaitijiang, Adjacent stimulation and measurement patterns considered harmful. *Physiol. Meas.* **32**, 731–744 (2011).
42. C. Xu, X. Dong, X. Shi, F. Fu, W. Shuai, R. Liu, F. You, "Comparison of drive patterns for single current source EIT in computational phantom," in *2008 2nd International Conference on Bioinformatics and Biomedical Engineering* (IEEE, 2008), pp. 1500–1503.
43. O. Luppi Silva, R. Gonzalez Lima, T. Castro Martins, F. Silva de Moura, R. Seiji Tavares, M. Sales Guerra Tsuzuki, Influence of current injection pattern and electric potential measurement strategies in electrical impedance tomography. *Control Eng. Pract* **58**, 276–286 (2017).
44. H. Wang, G. Xu, S. Zhang, W. Yan, Optimized excitation mode for generalized back projection algorithm in 3-D EIT. *IEEE Trans. Magn.* **51**, 1–4 (2015).
45. S. Russo, S. Nefti-Meziani, N. Carbonaro, A. Tognetti, A quantitative evaluation of drive pattern selection for optimizing EIT-based stretchable sensors. *Sensors* **17**, 1999 (2017).
46. W. R. Lionheart, K. Paridis, A. Adler, "Resistor networks and transfer resistance matrices," in *Proceedings of the 13th International Conference on Biomedical Applications of Electrical Impedance Tomography* (IOP Publishing, 2012), pp. 23–25.
47. H. Zhang, A. Kalra, A. Lowe, Y. Yu, G. Anand, A hydrogel-based electronic skin for touch detection using electrical impedance tomography. *Sensors* **23**, 1571 (2023).
48. M. Abdelwahed, L. Zerioul, A. Pitti, O. Romain, Using novel multi-frequency analysis methods to retrieve material and temperature information in tactile sensing areas. *Sensors* **22**, 8876 (2022).
49. D. Hardman, T. G. Thuruthel, F. Iida, Tactile perception in hydrogel-based robotic skins using data-driven electrical impedance tomography. *Mater. Today Electron.* **4**, 100032 (2023).
50. F. Pennati, A. Angelucci, L. Morelli, S. Bardini, E. Barzanti, F. Cavallini, A. Conelli, G. Di Federico, C. Paganelli, A. Aliverti, Electrical impedance tomography: From the traditional design to the novel frontier of wearables. *Sensors* **23**, 1182 (2023).
51. Y. Zhang, C. Harrison, "Tomo: Wearable, low-cost electrical impedance tomography for hand gesture recognition," in *UIST '15: Proceedings of the 28th Annual ACM Symposium on User Interface Software & Technology* (Association for Computing Machinery, 2015), pp. 167–173.
52. D. Hardman, T. George Thuruthel, F. Iida, Self-healing ionic gelatin/glycerol hydrogels for strain sensing applications. *NPG Asia Mater.* **14**, 11 (2022).
53. K. Paulson, W. Lionheart, M. Pidcock, Optimal experiments in electrical impedance tomography. *IEEE Trans. Med. Imaging* **12**, 681–686 (1993).
54. S. L. Brunton, J. N. Kutz, K. Manohar, A. Y. Aravkin, K. Morgansen, J. Klemisch, N. Goebel, J. Buttrick, J. Poskin, A. W. Blom-Schieber, T. Hogan, D. McDonald, Data-driven aerospace engineering: Reframing the industry with machine learning. *AIAA J.* **59**, 2820–2847 (2021).
55. M. Soori, B. Arezoo, R. Dastres, Artificial intelligence, machine learning and deep learning in advanced robotics, a review. *Cogn. Robot.* **3**, 54–70 (2023).
56. S. Tian, F. Ebert, D. Jayaraman, M. Mudigonda, C. Finn, R. Calandra, S. Levine, "Manipulation by feel: Touch-based control with deep predictive models," in *2019 International Conference on Robotics and Automation (ICRA)* (IEEE, 2019), pp. 818–824.
57. J. Zhu, J. C. Snowden, J. Verdejo, E. Chen, P. Zhang, H. Ghaednia, J. H. Schwab, S. Mueller, "EIT-kit: An electrical impedance tomography toolkit for health and motion sensing," in *UIST '21: The 34th Annual ACM Symposium on User Interface Software and Technology* (Association for Computing Machinery, 2021), pp. 400–413.
58. A. Adler, W. R. B. Lionheart, Uses and abuses of EIDORS: An extensible software base for EIT. *Physiol. Meas.* **27**, S25–S42 (2006).
59. T. Someya, T. Sekitani, S. Iba, Y. Kato, H. Kawaguchi, T. Sakurai, A large-area, flexible pressure sensor matrix with organic field-effect transistors for artificial skin applications. *Proc. Natl. Acad. Sci. U.S.A.* **101**, 9966–9970 (2004).
60. Q. Hua, J. Sun, H. Liu, R. Bao, R. Yu, J. Zhai, C. Pan, Z. L. Wang, Skin-inspired highly stretchable and conformable matrix networks for multifunctional sensing. *Nat. Commun.* **9**, 244 (2018).
61. S. Sundaram, P. Kellnhofer, Y. Li, J.-Y. Zhu, A. Torralba, W. Matusik, Learning the signatures of the human grasp using a scalable tactile glove. *Nature* **569**, 698–702 (2019).
62. W. W. Lee, Y. J. Tan, H. Yao, S. Li, H. H. See, M. Hon, K. A. Ng, B. Xiong, J. S. Ho, B. C. Tee, A neuro-inspired artificial peripheral nervous system for scalable electronic skins. *Sci. Robot.* **4**, eaax2198 (2019).
63. D. Hu, F. Giorgio-Serchi, S. Zhang, Y. Yang, Stretchable e-skin and transformer enable high-resolution morphological reconstruction for soft robots. *Nat. Mach. Intell.* **5**, 261–272 (2023).
64. D. Zhong, C. Wu, Y. Jiang, Y. Yuan, M. Kim, Y. Nishio, C.-C. Shih, W. Wang, J.-C. Lai, X. Ji, T. Z. Gao, Y.-X. Wang, C. Xu, Y. Zheng, Z. Yu, H. Gong, N. Matsuhisa, C. Zhao, Y. Lei, D. Liu, S. Zhang, Y. Ochiai, S. Liu, S. Wei, J. B.-H. Tok, Z. Bao, High-speed and large-scale intrinsically stretchable integrated circuits. *Nature* **627**, 313–320 (2024).
65. L. Nicholls, D. Hardman, F. Iida, "Multi-touch recognition of hydrogel-based e-skins using real-world eit datasets," in *2024 IEEE 7th International Conference on Soft Robotics (RoboSoft)* (IEEE, 2024), pp. 103–108.

Acknowledgments

Funding: This work was supported by the Samsung Global Research Outreach Program (GRO G118293 to F.I.), the Royal Society research grant RGS\R1\231472 to T.G.T., and EPSRC DTP EP/R513180/1 to D.H. **Author contributions:** All authors conceptualized the study and wrote the paper. D.H. performed all fabrication and experiments. D.H. and T.G.T. performed the data analysis. D.H. created the figures. **Competing interests:** The authors declare that they have no competing interests. **Data and materials availability:** All data needed to support the conclusions of this manuscript are included in the main text or Supplementary Materials. The data for this study have been deposited in databases https://doi.org/10.5281/zenodo.15387404 and https://github.com/DSHardman/InfoStructuring.

Submitted 3 May 2024
Accepted 13 May 2025
Published 11 June 2025
10.1126/scirobotics.adq2303

Science Robotics

Multimodal information structuring with single-layer soft skins and high-density electrical impedance tomography

David Hardman, Thomas George Thuruthel, and Fumiya Iida

Sci. Robot. **10** (103), eadq2303. DOI: 10.1126/scirobotics.adq2303

Science Robotics (ISSN 2470-9476) is published by the American Association for the Advancement of Science. 1200 New York Avenue NW, Washington, DC 20005. The title *Science Robotics* is a registered trademark of AAAS.